For the finite arrays, the transmission coefficient is based on the computed near field at point A on the array axis (Fig. 1(i)), at a distance of approximately $4a$ from the aperture plane. At

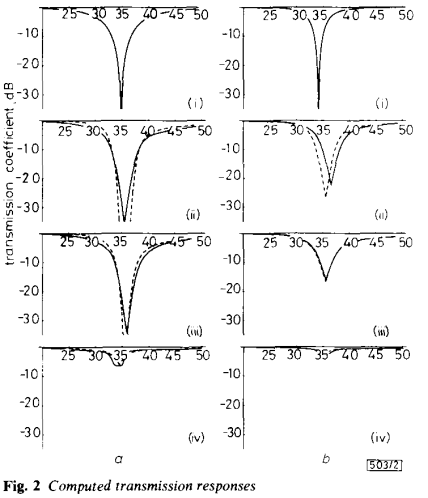

Fig. 2 *Computed transmission responses*
a $p = 4{\cdot}50$ mm
b $p = 6{\cdot}00$ mm
(i)–(iv): see text

points closer to the aperture, the transmission coefficient is very sensitive to numerical errors in the computed phase of the near field. Three arrays, with radii of curvature $r = \infty$, $2a$ and a, are considered. Fig. 2(ii) shows transmission curves for the finite planar array ($r = \infty$) of size 15×11 and 11×11 dipoles, corresponding to $p = 4{\cdot}50$ mm and $p = 6{\cdot}00$ mm, respectively. (The number of elements in the two arrays are different so that the aperture size in the E-plane remains the same, approximately $7{\cdot}4\lambda$ near the resonance frequency.) In the computations, mutual coupling effects from all elements within a sphere of radius 25 mm are included: this means five elements on all sides are included for the array with $p = 4{\cdot}50$ mm and three elements for the array with $p = 6$ mm. The broken curve shows the transmission coefficient computed without taking into account mutual coupling between the elements. As the Figures indicate, mutual coupling effects result in a shift in the resonance frequency in addition to reducing the null depth in the transmission curve. (For normal incidence, without mutual coupling between elements, the position of the transmission null is independent of periodicity.) The effect of coupling is more significant in the array with $p = 4{\cdot}50$ mm, and the resonance is wider and deeper.

Fig. 2(iii) and (iv) show the transmission curves for two curved arrays with the same aperture size ($a \simeq 70$ mm) as the corresponding planar arrays, and with $r = 2a$ and $r = a$, respectively. Generally, for values of $r \geq 2a$, the transmission curve shows a deep null comparable to the finite planar array of the same size, and there is a small shift in the resonance frequency. For $r < 2a$ the null steadily fills up until, for the nearly semi-circular cylindrical case (Fig. 2(iv)), the array is almost transparent, the null being only 6 dB deep for the closely spaced array and even less when $p = 6{\cdot}0$ mm. For the array with $p = 4{\cdot}5$ mm, the 'null' appears broad, owing to the widely different angles of incidence on the dipoles close to the axis. Because the angle of incidence varies across the array surface, different dipoles resonate at different frequencies, although the shift in resonance frequency with angle of incidence is small for the TM case considered here.

On a curved array, excited by an incident TM plane wave, the effect of mutual coupling varies across the array surface. For a finite planar array, mutual coupling effects can be accounted for by including the contribution from all elements within a fixed radius. This method does not work for the curved array where the contribution to the incident field from high currents in elements several periods away can be more significant than the near field from weakly-excited adjacent dipoles. For example, in the cylindrical array considered here, the contribution to the incident field at the edge dipole from the elements at the centre of the array is stronger than the field from closer neighbours, for the direction of incidence shown. This requires a specification on the value of the incident field contribution from a given element rather than including the effect of all dipoles within a fixed radius. The array structure and direction of incidence often provides a clue as to which elements are to be included in the computation. In the present analysis, all field contributions that together account for over 95% of the total input field at the dipole centre are included.

Close to (but not at) the centre of the array, where the dipoles are nearly tangential to the incident field, the curvature of the array results in the current distribution in the dipoles becoming asymmetric, distorted by mutual coupling effects. This contrasts with the case of a planar array with similar periodicity where owing to array symmetry, mutual coupling alters the magnitude but not the shape of the current pattern significantly. Away from the centre, where the dipoles are at high angles with the direction of the incident field, the element excitation from the incident plane wave field is low and hence mutual coupling with more distant elements nearer the centre tends to have a proportionally even greater effect on the current distribution in these dipoles. With TE incidence (the dipoles would be rotated through 90° in the tangent planes), mutual coupling in curved surfaces is higher than in a planar array because there are then many more equally excited elements within a fixed radius of a given dipole than in the corresponding planar array with the same periodicity.

Acknowledgment: This work was supported by a grant from the UK Science and Engineering Research Council.

25th March 1993

B. Philips, E. A. Parker and R. J. Langley (*Electronic Engineering Laboratories, The University, Canterbury, Kent CT2 7NT, United Kingdom*)

Reference

1 ALLAM, A. M. M. A., and PARKER, E. A.: 'Application of Pocklington's equation to analysis of dipole frequency-selective surfaces of finite size', *IEE Proc. H*, 1987, **134**, pp. 521–526

NOVEL RECURSIVE ALGORITHM AND HIGHLY COMPACT SEMISYSTOLIC ARCHITECTURE FOR HIGH THROUGHPUT COMPUTATION OF 2-D DHT

P. K. Meher and G. Panda

Indexing terms: Signal processing, VLSI, Transforms, Algorithms

A recursive algorithm and a fully pipelined semisystolic CORDIC architecture for computing the 2-D discrete Hartley transform are proposed. The proposed architecture has nearly eight times the throughput rate and requires nearly (1/8)th the chip area compared with the existing CORDIC architecture [1].

Formulation of algorithm: The two-dimensional discrete Hartley transform (2-D DHT) of an array $[x(m, n)]$ of size $N \times N$ is defined as

$$X(k, l) = \sum_{m=0}^{N-1} \sum_{n=0}^{N-1} x(m, n) \operatorname{cas} \frac{2\pi}{N} (km + ln) \qquad (1)$$

for $k, l = 0, 1, \ldots, N-1$ and $\operatorname{cas} v = \cos v + \sin v$.

Expanding the arguments of the cas function of eqn. 1, we obtain

$$X(k, l) = \sum_{n=0}^{N-1} w(k, n)\left[\cos\frac{2\pi ln}{N} + \sin\frac{2\pi ln}{N}\right] \quad (2)$$

for

$$w(k, n) = \sum_{m=0}^{N-1}\left[x(m, n)\cos\frac{2\pi km}{N} + x(m, (N-n))\sin\frac{2\pi km}{N}\right] \quad (3)$$

where (.) denotes modulo N operation.

The 2-D DHT is envisaged as being computed in two distinct stages. In the first stage, the intermediate output $[w(k, n)]$, for $k, n = 0, 1, \ldots, N-1$, is to be computed. The desired DHT components are to be computed in the second stage. The recursions in the processing elements (PEs) for both stages are given below.

Recursions of stage 1:

$$\begin{bmatrix} w(k, n) \\ w((N-k), N-n) \end{bmatrix} = \bar{R}^k[\ldots \bar{R}^k[\bar{R}^k u_1(L, n) + u_1(L-1, n)]\ldots + u_1(1, n)] + u_1(0, n) + R^k[\ldots R^k[R^k u_2(L, n) + u_2(L-1, n)]\ldots + u_2(1, n)] + u_2(0, n) \quad (4)$$

and

$$\begin{bmatrix} w((N-k), n) \\ w(k, N-n) \end{bmatrix} = \bar{R}^k[\ldots \bar{R}^k[\bar{R}^k u_2(L, n) + u_2(L-1, n)]\ldots + u_2(1, n)] + u_2(0, n) + R^k[\ldots R^k[R^k u_1(L, n) + u_1(L-1, n)]\ldots + u_1(1, n)] + u_1(0, n)\} \quad (5)$$

for $k, n = 0, 1, \ldots, L$. $L = (N-1)/2$, where N is assumed to be odd. (If N is even, the limits of k and n may be altered accordingly.) $w(k, N)$, for $k = 0, 1, \ldots, N-1$, are redundant, and may be ignored.

$$u_1(m, n) = \begin{bmatrix} x(m, n) \\ x(m, (N-n)) \end{bmatrix} \qquad 0 \le m, n \le L \quad (6a)$$

$$u_2(m, n) = \begin{bmatrix} x(N-m, n) \\ x(N-m, (N-n)) \end{bmatrix} \qquad \begin{matrix} 1 \le m \le L \\ 0 \le n \le L \end{matrix} \quad (6b)$$

and

$$u_2(0, n) = [0 \quad 0]^T \qquad 0 \le n \le L \quad (6c)$$

The rotation operators are given by

$$R^k = \begin{bmatrix} \cos(\alpha k) & -\sin(\alpha k) \\ \sin(\alpha k) & \cos(\alpha k) \end{bmatrix}$$

$$\bar{R}^k = \begin{bmatrix} \cos(\alpha k) & \sin(\alpha k) \\ -\sin(\alpha k) & \cos(\alpha k) \end{bmatrix}$$

and

$$\alpha = \frac{2\pi}{N} \quad (7)$$

Recursions of stage 2:

$$X(k, l) = Y_1(k, l) + Y_2(k, l) \qquad 0 \le k, l \le N-1 \quad (8)$$

where

$$Y(k, l) = \begin{bmatrix} Y_1(k, l) \\ Y_2(k, l) \end{bmatrix} = R^l[\ldots R^l[R^l z(k, L) + z(k, L-1)] + \cdots + z(k, 1)] + z(k, 0) \quad (9a)$$

and

$$Y(k, N-l) = \begin{bmatrix} Y_1(k, (N-1)) \\ Y_2(k, (N-1)) \end{bmatrix} = \bar{R}^l[\ldots \bar{R}^l[\bar{R}^l z(k, L) + z(k, L-1)] + \cdots + z(k, 1)] + z(k, 0) \quad (9b)$$

for $k = 0, 1, \ldots, N-1$, and $l = 0, 1, \ldots, L$, where

$$z(k, n) = \begin{bmatrix} w(k, n) \\ w(k, N-n) \end{bmatrix} \qquad \begin{matrix} 0 \le k \le N-1 \\ 1 \le n \le L \end{matrix} \quad (10a)$$

and

$$z(k, 0) = [w(k, 0)0]^T \qquad 0 \le k \le N-1 \quad (10b)$$

Proposed structure: It consists of three layers of linear systolic arrays placed one over the other, where each layer consists of $(L+1)$ arrays placed one over the other, where each layer consists of $(L+1)$ arrays. Arrays of the middle layer are termed the input arrays and those of outer layers, output arrays. Each of the input arrays and the output arrays consists of $(L+1)$ locally connected PE-Is (Fig. 1*b*) and PE-IIs (Fig. 2*b*), respectively. Each output array is also connected to an adder to compute the 2-D DHT components from $Y_1(k, l)$ and $Y_2(k, l)$ according to eqn. 8. Structures of the middle layer and an outer layer are depicted in Figs. 1*a* and 2*a*, respectively. Input arrays are oriented orthogonally with respect to the

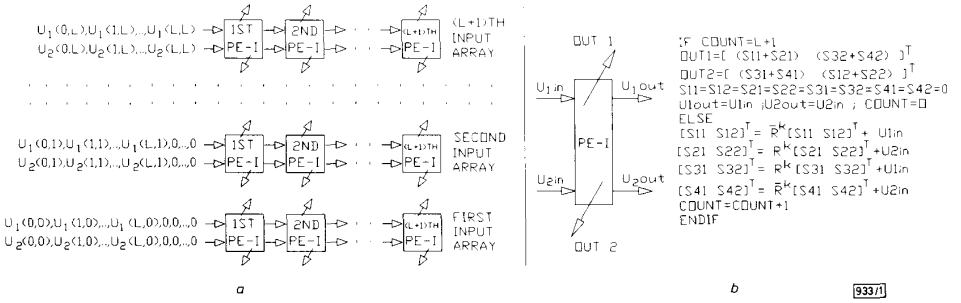

Fig. 1 *Structure and function of a middle layer and the $(k+1)$th PE-I of an input array*

a Middle layer

b $(K+1)$th PE-I of an input array

The phase elements corresponding to the rotation operators R^k and $\bar{R}^k$ are stored in the local memory

output arrays in such a manner that the PEs of the nth input array ($n = 1, 2, \ldots, L + 1$) remain sandwiched between

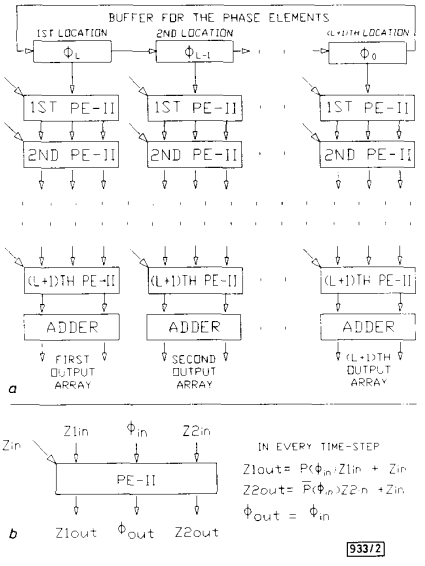

Fig. 2 *Structure of outer layer and PE-II*

a Outer layer

b PE-II

In every time step the phase elements ϕ_i, $i = 0, 1, \ldots, L$ are transferred to the adjacent locations towards the right: $P(\phi_i) = R^i$ and $\bar{P}(\phi_i) = \bar{R}^i$.

$(L + 2 - n)$th PEs of the output arrays. Elements of the nth columns ($n = 1, 2, \ldots, L + 1$) of $[u_1(k, n)]$ and $[u_2(k, n)]$ (matrices of size $(L + 1) \times (L + 1)$ obtained according to eqn. 6) are fed serially to the nth input array, in reverse order, staggered by one time step with respect to the corresponding elements of the $(n + 1)$th columns. One time step is considered as the time required to perform a pair of phase rotations followed by two real additions. In every $(L + 1)$ time steps each PE-I provides an upward and a downward output, which form the input for the next $(L + 1)$ time steps, to its neighbouring PE-IIs existing in the outer layers.

Hardware and throughput considerations: The proposed architecture requires $(L + 1)^2$ PE-Is and $2(L + 1)^2$ PE-IIs. It computes the first set of 2-D DHTs in $4L + 2$ time steps and successive sets in an interval of $L + 1$ time steps. If the scheme of the CORDIC implementation of phase rotation the same as that of Reference 1 is employed in the PEs of the proposed structure, then the hardware requirement of a PE-I and a PE-II would, respectively, be four times and two times that of a PE of Reference 1. As a whole, the proposed structure would require nearly the same amount of hardware as the structure of Reference 1, and the duration of a time step would remain nearly the same for both the structures. However, the present structure would have a throughput rate of $\sim[2/(N$ time steps)], and would require a chip area of $O(N/2 \times N/2)$, whereas the structure of Reference 1 has a throughput rate of $\sim[1/(4N$ time steps)] and chip area $O(2N \times N)$.

Conclusion: A recursive algorithm and an efficient architecture have been proposed for computing the 2-D DHT. Besides, the desirable features such as modularity, regular and local connections, and full pipelineability, the proposed structure has a special advantage in that it neither requires any extra hardware nor any extra time for transposition of the intermediate output $[w(k, n)]$. Transposition is avoided by orthogonal alignment of output arrays with respect to input arrays. Compactness of the structure is achieved by its 3-D nature. Both high throughput as well as compactness have, however, been possible due to the massive parallelism inherent with the proposed algorithm. For a more hardware efficient realisation, a pair of phase rotations of the form $R^n u$ and $\bar{R}^n v$, occurring in eqns. 4, 5, and 9, may be performed by a single CORDIC circuit, similar to one suggested in Reference 2 (page 272), where the unnormalised rotations for one phase rotation may be performed simultaneously with the normalisations corresponding to the other.

8th February 1993

P. K. Meher* and G. Panda (*Department of A.E. & I.E., Regional Engg. College, Rourkela- 769 008, India*)

P. K. Meher is on leave from the Dept. of Physics, Govt. College, Rourkela, India)

References

1 CHANG, L. W., and LEE, S. W.: 'Systolic arrays for the discrete Hartley transform', *IEEE Trans.*, 1991, **SP-39**, (11), pp. 2411–2418

2 DEWILDE, P., DEPRETTERE, E., and NOUTA, R.: 'Parallel and pipelined VLSI implementation of signal processing algorithms', in KUNG, S. Y., WHITEHOUSE, H. J., and KAILATH, T. (Eds.): 'VLSI and modern signal processing' (Englewood Cliffs, NJ: Prentice Hall), pp. 257–276

HIGH PERFORMANCE WIDEBAND ANALOGUE TIME SHIFTER

S. Lucyszyn, I. D. Robertson and A. H. Aghvami

Indexing terms: Delay lines, Phase shifters

A proof-of-concept analogue reflection-type time shifter is presented for the first time. The measured results for an experimental hybrid realisation, having a centre frequency of 750 MHz, demonstrate a high performance over a 40% bandwidth. The design is totally compatible with monolithic technology and suitable for both microwave and millimetre wave applications.

Introduction: High performance variable time shifters are employed wherever ideal tunable delay lines are required. Examples include: adaptive beam-forming networks for wideband phased array antennas, phased array antenna emulators [1], phase matching networks for radar and ECM subsystem interconnects [2], and building blocks in future analogue signal processing architectures.

Common classes of time shifter, which are compatible with both hybrid microwave integrated circuit (MIC) and monolithic MIC technology, are: digital switched-line, analogue loaded-line, and digital reflection-type. The concept of an analogue reflection-type time shifter (RTTS) was only recently introduced [3]. Here, the simulated results of an X-band design, having a maximum relative phase shift of 90°, at a centre frequency of 10 GHz, demonstrated that a high performance was possible over at least a 40% bandwidth. The first measured results for an experimental realisation of this time shifter are presented in this Letter.

Realisation: The topology of an ideal analogue RTTS simply consists of a 3 dB quadrature directional coupler with identical series L-C tuned circuit reflection terminations connected to its coupled and direct ports and the output taken from the isolated port: this topology has traditionally been associated with reflection-type phase shifters [4]. An analogue RTTS, having a centre frequency of 750 MHz, was realised using microstrip techniques, employing a folded four-finger Lange coupler. The variable capacitors were implemented with mesa-type chip varactor diodes, having abrupt junction characteristics. Each inductor was realised with a single long wire. A photograph of the $1{\cdot}0 \times 1{\cdot}0\,\text{inch}^2$ time shifter is shown in Fig. 1 and the corresponding model is illustrated in Fig. 2.